

Contrast enhanced imaging in the sea: Application of the optical transfer function for image reconstruction

Frank Ahrenberg, Stefan Harsdorf, Joerg Niehues, and Rainer Reuter

Carl von Ossietzky Universität Oldenburg
26111 Oldenburg, Germany

email: {harsdorf/reuter}@las.physik.uni-oldenburg.de

ABSTRACT

Range gated imaging is a well-known technique to enhance the performance of underwater video imaging. In accordance with the concept of lidar a short laser pulse is used as the light source of a camera with an exposure time in the range of a few nanoseconds. A synchronisation of laser emission and camera gate-on time allows to suppress the backscattered light from the water column between detector and object and to record only the light backscattered by the object. This generally results in a contrast enhanced video image.

The image from the object is transmitted through a scattering medium, i. e. the water between object and detector. The undisturbed image of the object is therefore convoluted with the optical transfer function (OTF) of the camera and the water. This results in an attenuation especially of high spatial frequencies and hence to a loss of contrast in the image. The detector can be regarded as a constant, but the OTF of the water is strongly dependent on its optical properties, mainly the amount of suspended particles.

The OTF of different water types has been measured in a 10 m laboratory tank using a range gated camera. The system consists of an Nd:YAG laser (532 nm, 4 ns pulse width) and an intensified CCD camera with a 5 ns minimum gate time.

A direct image deconvolution using the OTF is mostly impossible, since the measured OTF and video images are obscured by noise. To overcome this problem, two techniques for image reconstruction, i.e. the Monte Carlo approximation and the wavelet transformation and filtering, have been adapted, tested and compared using a computer simulation of image recording. Preliminary results from computer simulations and from experiments in the laboratory are presented.

1. INTRODUCTION

Today, sonars are the standard tools in underwater imaging, because of their longer range compared with optical instruments in water. However, optical instruments are still the only means for imaging of small objects. Because of shorter wavelengths compared to light, the geometric resolution of acoustical images is mostly insufficient to detect relevant details of objects on the seafloor. Examples of such objects are small leaks in barrels sunken to the seafloor in the field of pollution

monitoring, and investigations of benthic algae for ecological monitoring.

Limitations of the performance of conventional underwater video cameras are due to scattering and absorption of light in turbid waters. To enhance image quality and visibility range, new methods and techniques have been developed for the illumination of objects and image recording [Gilbert, 1970; Svensson et al., 1981; Christie and Kvasnik, 1996].

2 OPTICAL TRANSFER FUNCTION IN NATURAL WATERS

The optical transfer function (OTF) is a well defined measure for the performance of an imaging instrument. It can be calculated as the Fourier transform of the point spread function (PSF). The PSF describes the image of a spatial delta pulse, i.e. a point source with Lambertian emission properties. It can be shown that the PSF is equivalent to the beam spread function (BSF) [Gordon, 1994].

As a complex function the OTF can be expressed as the product of the modulation transfer function (MTF) and the phase transfer function (PTF). In underwater imaging the PSF can be approximated by symmetric functions. Then the PTF which describes the phase shift of spatial frequencies can be neglected. The MTF represents the reduction of the amplitudes of the different spatial frequencies.

The MTF of an imaging instrument includes both the MTF of the water column and of the detector. The detector MTF is the same in all images and can be measured. The MTF of the water column, however, is a function of the water and its dissolved and particulate constituents. The value of the MTF depends on the length of the water column. The attenuation coefficient c of the water can be directly calculated from the BSF. The absorption coefficient a can be estimated from the PSF for short ranges [Mertens and Replogle, 1977]. With c and a the scattering coefficient b is also known. The relation of the beam attenuation coefficient and substances in the water such as particulate matter, yellow substance and algae, has been described e.g. by Barth et al. [1997]. A transform relation between the PSF and the volume scattering function $\beta(\theta)$ with the scattering angle θ has been developed by Wells [1969]. It includes multiple scattering and is valid in the small angle region of

$\beta(\theta)$. Measurements of the PSF especially in coastal waters have been reported by [Voss, 1997].

3. METHOD

3.1 Range gated image recording

An underwater image can be regarded as a linear superposition of three different components, (i) backscattering from the water body and from the target, and (ii) light backscattered by the target and (iii) forward scattered by the water body [Jaffe, 1986].

The first component does not include any information about the object because it has never reached it. Range gated imaging is a technique which allows to separate this light from the two other components. Because of the use of a laser emitting short pulses and according to the concept of lidar, it arrives at the camera prior to the other two components. A laser pulse length and minimum camera gate time of a few nanoseconds allows to fade out this light, and to record only the light reflected by the object. This generally results in a contrast enhanced video image.

The second component consists of the light following a direct trace from the target to the detector without being scattered in the intervening water. Therefore, this component forms a sharp image of the observed object. The image quality is only influenced by the optical transfer function (OTF) of the CCD camera. Image intensity and signal-to-noise ratio are determined by the attenuation of light in the water.

The third component consists of the light reflected by the object and then forward scattered at small angles between object and camera. It reaches the detector approximately at the same time as the second component. Therefore it is not possible to separate the remaining two components by their time of flight. The result is a blurred image of the object. It can be calculated as a convolution of the original image and the PSF that describes the optical characteristics of the water.

The recorded image is modulated by the OTF of the water and the CCD camera system. The unblurred image can be reconstructed with image processing if the PSF are known.

3.2 Image reconstruction

3.2.1 Monte Carlo approximation

Range gating suppresses the backscattered light from the water column, and the direct contribution from the object and the forward scattered components are registered. If the imaging system is considered to be linear and shift-invariant, the intensity distribution of the image $I(x,y)$ can be described as the result of the convolution

$$I(x,y) = O(x,y) * \text{PSF}(x,y) + N(x,y) ,$$

where $\text{PSF}(x,y)$ is the point spread function of the camera and the water, and $N(x,y)$ is an additive noise term.

Image data are degraded with noise. Therefore, the inverse problem cannot be solved analytically., and numerical approaches are required [Ting-lu and Hai, 1994]. The Monte Carlo method is a widely used statistical tool. For this method it is necessary to realise a statistical model which includes all possible solutions of the problem. A sample representing the solution is built up by a large number of trials which are selected randomly from probabilistic and deterministic laws. Advantages of the Monte Carlo deconvolution algorithm are:

- there is no need for an analytical description of the output
- the output has infinite flexibility regarding fluctuations: edge gradients and linear resolution distances are not constrained by the bandwidth
- all desired constraints, e.g. positivity, upper bound etc., can easily be integrated in the statistical model

The object can be regarded as a composition of a large number of point sources. The water column is assumed to be homogeneous. Hence, the PSF is the same at any position (x,y) ; the system is space-invariant. The image detected by the camera $I(x,y)$ can be assumed to result from randomly distributed point spread functions. Simultaneously to this allocation of smeared point sources in the image plane the intensities of these sources d^i will be stored in a second matrix with the function:

$$O(x,y) = d^i \cdot \delta(x-k, y-l) \quad k \in N, l \in M$$

where δ is the Dirac delta function defined by

$$\delta(x-k, y-l) = \begin{cases} 1 & \text{if } (x-k) \text{ and } (y-l) = 0 \\ 0 & \text{else} \end{cases}$$

The image space $I^0(x,y)$ and the object space $O^0(x,y)$ are composed of empty resolution cells. Within the image dimensions, in horizontal direction N and in vertical direction M two numbers k and l are randomly chosen. These numbers define the location for allocating a blurred point source in the image plane. The intensity of the point source is found randomly.

For the first point source localised at the resolution cell (x_k, y_l) with intensity d^1 the formation of the image is found by

$$I^1(x_n, y_m) = I^0(x,y) + d_{k,l}^1 \cdot \text{PSF}(x_n - x_k, y_m - y_l) \\ n = 1 \dots N, \quad m = 1 \dots M ,$$

and for the distribution in the object space by

$$O^1(x_n, y_m) = O^0(x,y) + d_{k,l}^1 \cdot \delta(x-k, y-l) .$$

For the second point source localised at the resolution cell (x_k, y_l) with intensity d^2 the approximations of the image and the object are given by

$$I^2(x_n, y_m) = I^1(x,y) + d_{k,l}^2 \cdot \text{PSF}(x_n - x_k, y_m - y_l)$$

and

$$O^2(x_n, y_m) = O^1(x,y) + d_{k,l}^2 \cdot \delta(x-k, y-l)$$

If all point sources are distributed such that the sum of the differences between the measured image $I(x,y)$ and the simulated image $I^i(x,y)$ is minimised, i.e.

$$\sum_m^M \sum_n^N |I(x, y) - I'(x, y)| = \varepsilon = \min ,$$

then the image for the k 'th allocation has formed to

$$I^k(x_n, y_m) = I^{k-1}(x, y) + d_{k,l}^k \cdot \text{PSF}(x_n - x_k, y_m - y_l)$$

and the object to

$$O^k(x_n, y_m) = O^{k-1}(x, y) + d_{k,l}^k \cdot \delta(x - k, y - l)$$

If ε is sufficiently small, the simulated image $I^k(x, y)$ corresponds to the sampled image $I(x, y)$ and $O^k(x, y)$ represents the restored image.

3.2.2 The Richardson-Lucy method using the wavelet transformation for noise suppression

Another efficient method for image reconstruction is the Richardson-Lucy method using the wavelet transformation for noise suppression [Richardson, 1972; Starck and Murtagh, 1994]. This method applies an iterative approach

$$O^{i+1}(x, y) = O^i(x, y) \left[\left(\frac{I^i(x, y) + R^i(x, y)}{I^i(x, y)} \right) * \text{PSF}^T(x, y) \right]$$

with $I^i(x, y) = \text{PSF}(x, y) * O^i(x, y)$.

PSF^T is the transposed of the PSF and $O^i(x, y)$ is the current estimate of the object. $R^i(x, y)$ is the residual at iteration i , defined by

$$R^i(x, y) = I(x, y) - I^i(x, y) .$$

This residual contains two kinds of information: the statistically significant structures and, on the other hand, due to noise, statistically insignificant structures. With the wavelet transformation it is possible to extract the significant part of the residual. The wavelet transformation used here is implemented as a multi-resolution analysis. It is a special discrete version of the continuous wavelet transformation.

The multi-resolution analysis of a function $R(x)$ is generated by the decomposition of $R(x)$, defined as averages on different scales. $R(x)$ is supposed to be an element of the subspace V_0 . A hierarchy of subspaces is formed by $\dots V_2 \subset V_1 \subset V_0$.

The detailed information that is lost by the smoothing from V_j to V_{j+1} , is given by the orthogonal projection of $R(x)$ on a subspace W_j that W_j is orthogonal to V_j in V_{j+1} so that $W_j \oplus V_j = V_{j+1}$.

Generally, the sampled data $c_0(k)$ are defined as the scalar product

$$c_0(k) = \langle R(x), \Phi(x - k) \rangle$$

where $\Phi(x)$ is a scaling function corresponding to a low pass filter. The projection onto the subspaces V_j is defined by the scalar product $c_j(k)$ of $R(x)$ with dilated and translated versions of the scaling function $\Phi(x)$

$$c_j(k) = \frac{1}{2^{\left(\frac{j}{2}\right)}} \left\langle R(x), \Phi\left(\frac{x-k}{2^j}\right) \right\rangle$$

The scaling function has to satisfy the dilation equation:

$$\Phi(x) = \sqrt{2} \sum_{k \in Z} h(k) \cdot \Phi(2x - k)$$

where $h(k)$ is a discrete low pass filter associated with the scaling function. The dilation equation allows to calculate $c_{j+1}(k)$ from $c_j(k)$, with $j \geq 0$:

$$c_{j+1}(k) = \sum_l h(1-2k) c_j(l)$$

At each iteration the signal is smoothed and subsampled by a factor of two. The information loss by smoothing can be restored using the complementary subspace W_j of V_j in V_{j+1} . The projection onto this subspace is defined by the scalar product $w_j(k)$ of $R(x)$ with dilated and translated versions of the wavelet $\Psi(x)$:

$$w_j(k) = \frac{1}{2^{\left(\frac{j}{2}\right)}} \left\langle R(x), \Psi\left(\frac{x-k}{2^j}\right) \right\rangle$$

The wavelet $\Psi(x)$ also have to satisfy a dilation equation:

$$\Psi(x) = \sqrt{2} \sum_k g(k) \Psi(2x - k)$$

where $g(k)$ is a discrete high pass filter associated with the wavelet $\Psi(x)$.

Then $w_{j+1}(k)$ can be calculated from $c_j(k)$, with $j \geq 0$:

$$w_{j+1}(k) = \sum_l g(1-2k) c_j(l)$$

The set $\{c_p, w_1, w_2, \dots, w_p\}$ is the result of the wavelet analysis down to the wavelet plane $j=p$. The restoration of the original data requires the conjugated filters \tilde{h} and \tilde{g} to h and g . Then the restoration is performed with:

$$c_j(k) = \sum_{l \in Z} c_{j+1}(l) \cdot \tilde{h}(k-2l) + w_{j+1} \cdot \tilde{g}(k-2l)$$

As with the two-dimensional fast Fourier transformation one obtains a two-dimensional multiscale analysis by calculating the transformation in both dimensions. Therefore, the scaling function is represented by

$$\Phi(x, y) = \Phi(x) \cdot \Phi(y) ,$$

and one gets three wavelets, which include detailed information in the x and y directions and in the diagonal:

$$\Psi^x(x, y) = \Psi(x) \cdot \Phi(y)$$

$$\Psi^y(x, y) = \Phi(x) \cdot \Psi(y)$$

$$\Psi^{xy}(x, y) = \Psi(x) \cdot \Psi(y)$$

This leads to four sub-images:

$$c_{j+1}(k_x, k_y) = \sum_{l_x} \sum_{l_y} h(l_x - 2k_x) h(l_y - 2k_y) c_j(l_x, l_y)$$

$$w_{j+1}^x(k_x, k_y) = \sum_{l_x} \sum_{l_y} g(l_x - 2k_x) h(l_y - 2k_y) c_j(l_x, l_y)$$

$$w_{j+1}^y(k_x, k_y) = \sum_{l_x} \sum_{l_y} h(l_x - 2k_x) g(l_y - 2k_y) c_j(l_x, l_y)$$

$$w_{j+1}^{xy}(k_x, k_y) = \sum_{l_x} \sum_{l_y} g(l_x - 2k_x)g(l_y - 2k_y)c_j(l_x, l_y)$$

With the conjugated filters \tilde{h} and \tilde{g} , the synthesis can be calculated as

$$\begin{aligned} c_j(k_x, k_y) &= c_{j+1}(k_x, k_y)\tilde{h}(k_x - 2l_x)\tilde{h}(k_y - 2l_y) \\ &+ w_{j+1}^x(k_x, k_y)\tilde{g}(k_x - 2l_x)\tilde{h}(k_y - 2l_y) \\ &+ w_{j+1}^y(k_x, k_y)\tilde{h}(k_x - 2l_x)\tilde{g}(k_y - 2l_y) \\ &+ w_{j+1}^{xy}(k_x, k_y)\tilde{g}(k_x - 2l_x)\tilde{g}(k_y - 2l_y) \end{aligned}$$

The aim is to suppress the noise in the residual $R(x,y)$ derived from the Richardson-Lucy algorithm. Therefore, the standard deviation σ_0 of the noise in the image $I(x,y)$ is estimated. The wavelet transformation is linear. So the standard deviation σ_j of the noise at scale j can be approximated. For noise suppression the weighting function α is defined as:

$$\alpha(w_j(k_x, k_y), \sigma_j) = \begin{cases} 1 & \text{if } |w_j(k_x, k_y)| \geq p \cdot \sigma_j \\ 0 & \text{if } |w_j(k_x, k_y)| < p \cdot \sigma_j \end{cases}$$

where p determines the threshold level.

Multiplying each sub-image $\{w_j^x, w_j^y, w_j^{xy}\}$ with the weighting function α into the wavelet synthesis the significant residual $S(x,y)$ is obtained. The residual $R^i(x,y)$ can now be replaced by its significant part $S^i(x,y)$ so that a main part of the noise will be suppressed.

4. COMPUTER SIMULATIONS

4.1 Results of the Monte Carlo simulation

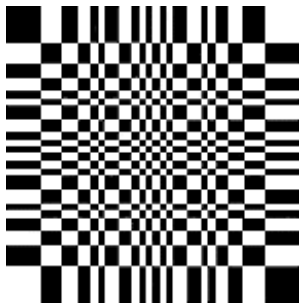


Fig. 1: Test pattern with $m_s=129.57$ and $q_s=1.46 \cdot 10^4$

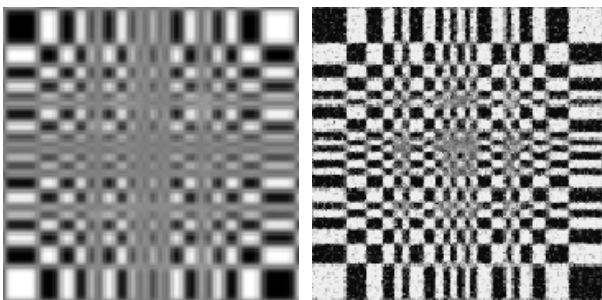


Fig. 2: Image reconstruction with the Monte Carlo method without noise. On the left: input image with $m_s=124.76$, $q_s=6.20 \cdot 10^3$. On the right: reconstructed image with $m_s=124.76$, $q_s=8.09 \cdot 10^3$.

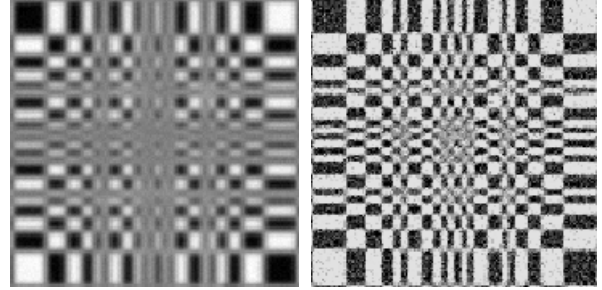


Fig. 3: Same as in Fig. 2, but with 5% random noise. On the left: input image with $m_s=128.72$, $q_s=5.89 \cdot 10^3$. On the right: reconstructed image with $m_s=143.27$, $q_s=7.60 \cdot 10^3$.

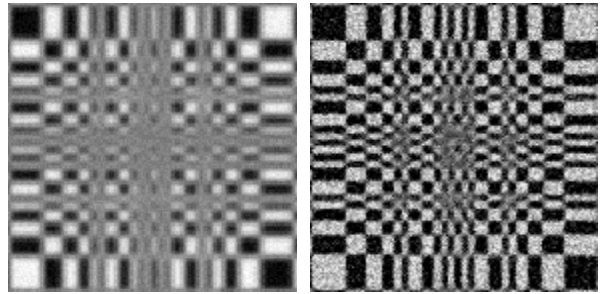


Fig. 4: Same as in Fig. 2, but with 10% random noise. On the left: input image with $m_s=128.64$, $q_s=5.40 \cdot 10^3$. On the right: reconstructed image with $m_s=101.25$, $q_s=5.91 \cdot 10^3$.

4.2 Results of the wavelet simulation

For the computer simulations the image $I(x,y)$ is generated by the convolution of a known PSF with a test pattern image. Gaussian noise with different intensities is added. The following two images show the test pattern and the generated image with 10% noise.

A wavelet which has been used for the noise suppression is the Daubechies wavelet D4. The coefficients of the corresponding high pass and low pass filters are given in the following table.

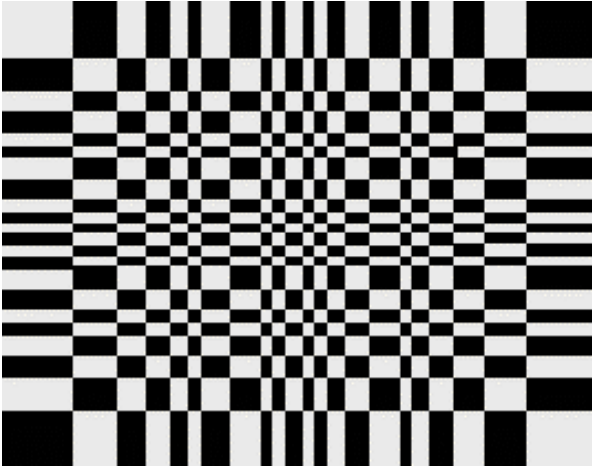


Fig. 5: Test pattern

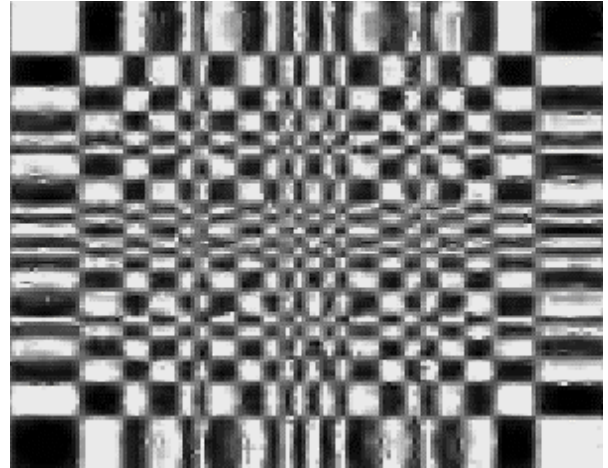


Fig. 7: Restoration with 5% noise and p=3

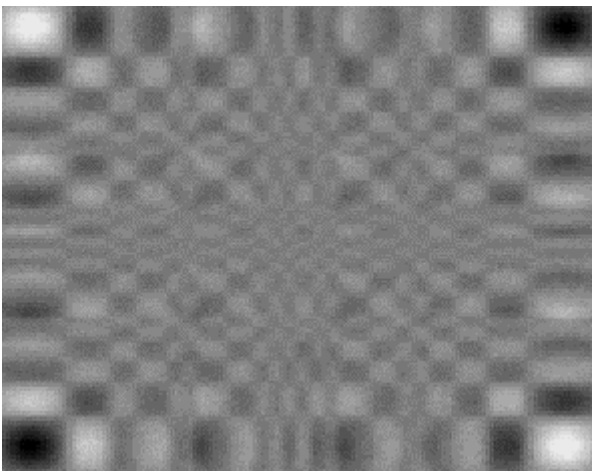


Fig. 6: Image of the test pattern

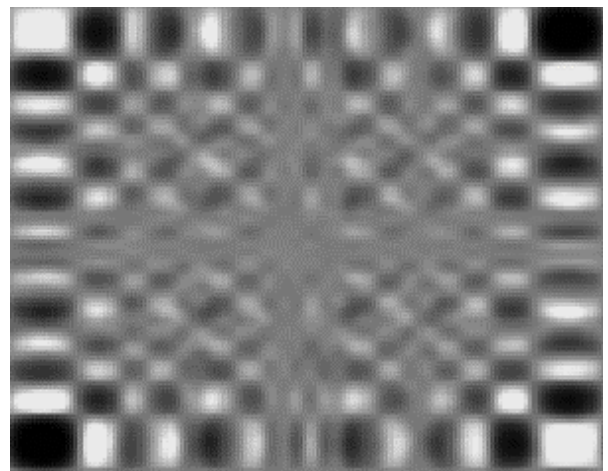


Fig. 8: Restoration with 10% noise and p=3

k	0	1	2	3	$k \neq 0,1,2,3$
$h(k)$	$\frac{1-\sqrt{3}}{4\sqrt{2}}$	$\frac{3-\sqrt{3}}{4\sqrt{2}}$	$\frac{3+\sqrt{3}}{4\sqrt{2}}$	$\frac{1+\sqrt{3}}{4\sqrt{2}}$	0
$g(k)$	$\frac{1-\sqrt{3}}{4\sqrt{2}}$	$-\frac{3-\sqrt{3}}{4\sqrt{2}}$	$\frac{3+\sqrt{3}}{4\sqrt{2}}$	$-\frac{1+\sqrt{3}}{4\sqrt{2}}$	0

With p set to 1 and 2, only 65% and 95% of the noise are eliminated, but more details are restored. The disadvantage is the appearance of artefacts related to noise. Figs. 9 and 10 show the restoration with 10% noise and p=1 and p=2.

The wavelet transformation is computed only for three wavelet plains ($j=1...3$), because the signal-to-noise ratio increases at lower scales of the image corresponding to higher wavelet plains. The threshold level for the noise is laid down with the factor p in the weighting function α . With Gaussian noise, about 99% of the noise is suppressed with p=3. Figs. 7 and 8 show the result of the restoration with 5% and 10% noise and p=3.

With decreasing signal-to-noise ratio in the image, the faintly visible small space frequencies are also suppressed. This effect can be seen in the centre of Fig. 8.

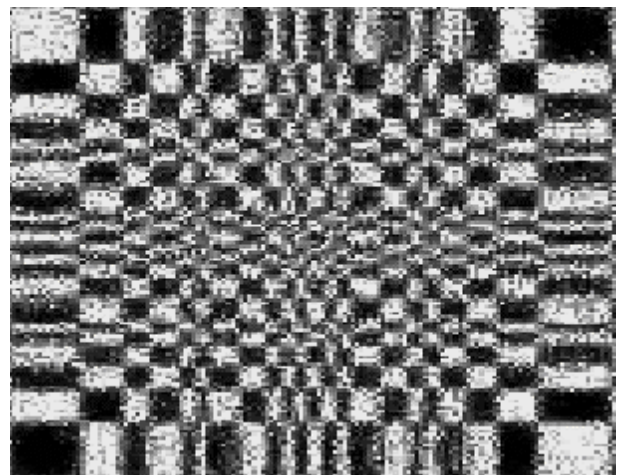


Fig. 9: Restoration with 10% noise and p=1

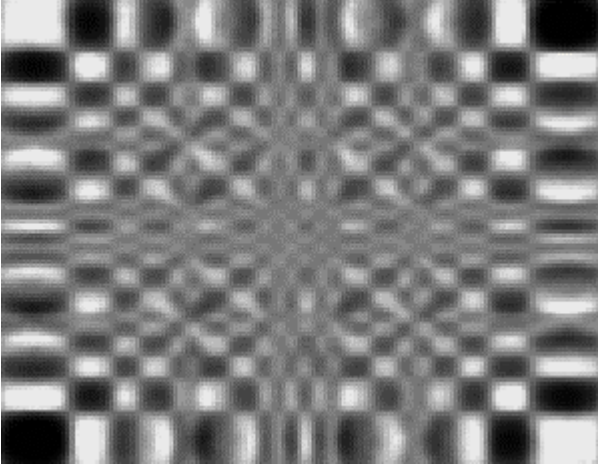


Fig 10: Restoration with 10% noise and $p=2$

5. EXPERIMENTAL RESULTS

5.1 Range gated video imaging

To determine the performance of range gated video, experiments have been carried out in a laboratory tank with 10 m length. Coastal water as typically found in the German Bight near Helgoland has been simulated concerning its absorbing and scattering properties.

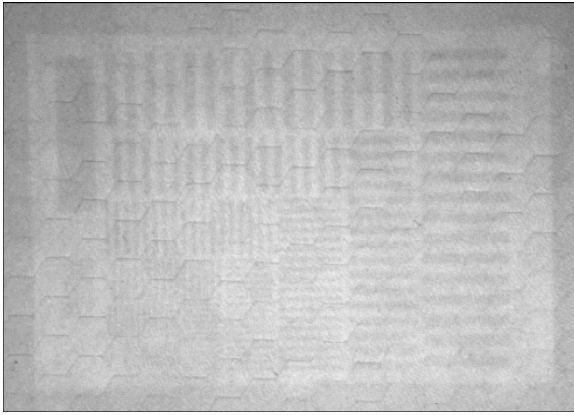


Fig. 11: Target at 10 m distance with gate time = ∞

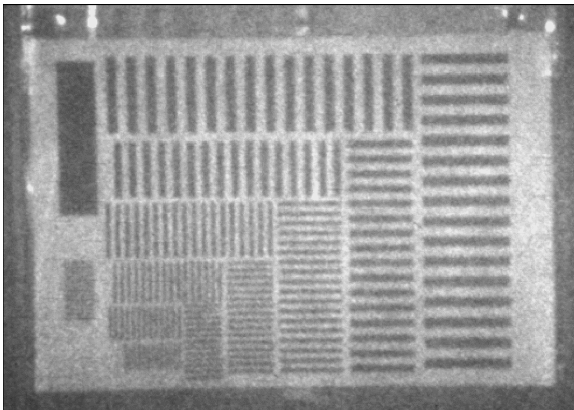


Fig. 12: Target at 10 m distance with gate time 5 ns

Figs. 11 and 12 show images of a test pattern in turbid water. In both cases the distance between camera and target was 10 m. As the light source the green emission of a doubled Nd:YAG laser (532 nm) was used. Fig. 1 shows the image recorded with an exposure time of the camera much longer than the pulse length and the time-of-flight of the laser pulse in the water. Therefore, the result is equivalent to a conventional underwater video image. Fig. 12 shows the result of the same experiment, however, with a gate-on time of 5 ns. The delay between laser emission and gate was chosen such that the light backscattered by the target reached the camera within the gate-on time. Hence, light backscattered by the water column has not been recorded. The images in Figs.11 and 12 demonstrate the contrast enhancement of a range gating imaging camera.

5.2 The modulation transfer function

The MTF measurement with bar-code targets is a well-known technique in the Fourier analysis of optical systems. The space invariance may be lost if a digital camera is used. Then the intensity distribution of the sampled image depends on the relative position of the PSF with respect to the sampling grid. In signal theory this effect is called aliasing. The counterpart in image analysis is the Moiré effect. To avoid aliasing, the target design proposed by [Sitter, Goddard, and Ferrel] was used. The modulation of the barpattern was chosen such that the overlap between spatial frequencies and their corresponding higher harmonics is minimised. Only the positive frequency components are of interest for determining the MTF. With the distance Δ between two neighbouring pixels in the sampling grid and the distance d for one modulation, the fundamental frequency of the bar pattern is given by

$$\frac{1}{d} = \frac{1}{(m+1)\Delta}, \quad \text{with } m = 1, 2, 3 \dots$$

With this modulation an overlap of the m 'th harmonic frequency (at the location $1/\Delta - m/d$) and the fundamental frequency for a number of discrete frequencies is possible. To avoid the overlap, fundamental frequencies are chosen, which are farthest from the overlap condition. They are found by examining the frequencies which are equidistant to the m 'th and the $m+1$ th harmonic alias-frequencies.

$$\frac{1}{d} - \left(\frac{1}{\Delta} - \frac{m+1}{d} \right) = \left(\frac{1}{\Delta} - \frac{m}{d} \right) - \frac{1}{d}$$

The left side of this equation is the distance between the fundamental and the $(m+1)$ 'th harmonic frequency, and the right side the distance between the fundamental and the m 'th harmonic frequency. The equation can be solved with respect to the fundamental frequency.

$$\frac{1}{d} = \frac{2}{(2m+3)\Delta} \quad \text{with } m = 1, 2, 3, \dots$$

With $1/d = k/N\Delta$, the number of circles in the bar pattern is given by

$$\bar{k} = \frac{2N}{2m+3} \quad \text{with } m = 1, 2, 3, \dots,$$

where the values of \bar{k} and N must be integer. With these results the bar-code targets were drawn for distances of 2.5, 5.0, 7.5 and 10 m with respect to the chosen magnification scales. The modulations differ in horizontal and vertical direction because of the different resolutions of the CCD camera. The next figure shows a bar-target designed for measurements at 10 m distance.

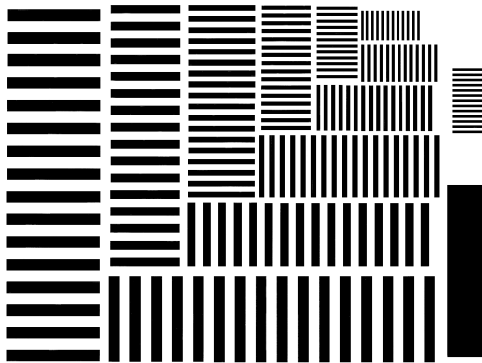


Fig. 13: Target for MTF measurement, designed for 10 m distance

The discrete Fourier transformation in combination with the modulation of the target leads to the system MTF H :

$$\left| H\left(\frac{1}{d}\right) \right| = \left| \frac{d \bar{I} |\bar{k}|}{N a L \text{sinc}(L/d)} \right|.$$

L represents the width of a white bar in the image, d the spatial period of the pattern, a the difference of irradiance between a black and a white area, and the Fourier transformation of the sampled image

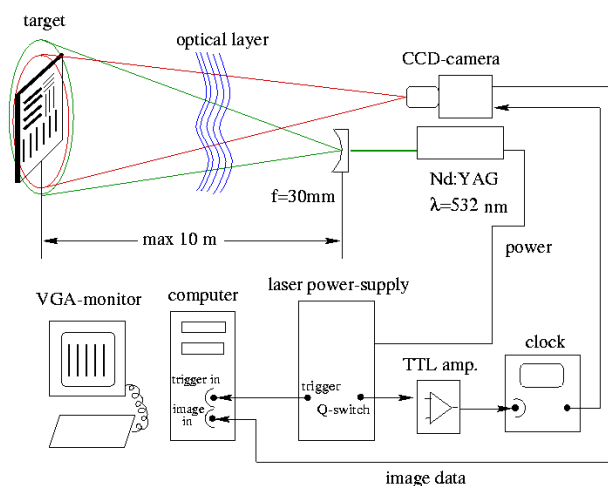


Fig. 14: Experimental setup for MTF measurements

The MTF was measured in a tank with the dimension $0.45 \text{ m} \times 0.45 \text{ m} \times 10 \text{ m}$. To simulate natural waters the tank was filled with de-ionised water and well defined algae samples. For simulating different types of water

bodies different types of algae at different concentrations were used. The target was illuminated with the 2nd harmonic of an Nd:YAG laser at 532 nm, with 160 mJ pulse energy and 4 ns pulse width. The beam divergence was adjusted to the camera field of view. The image was recorded with an intensified CCD camera and 5 ns gate-on time. The delay between laser emission and gate was chosen such that the light backscattered by the target reached the camera within the gate-on time. Images were recorded with 8 bit radiometric and 1.024×768 pixel resolution.

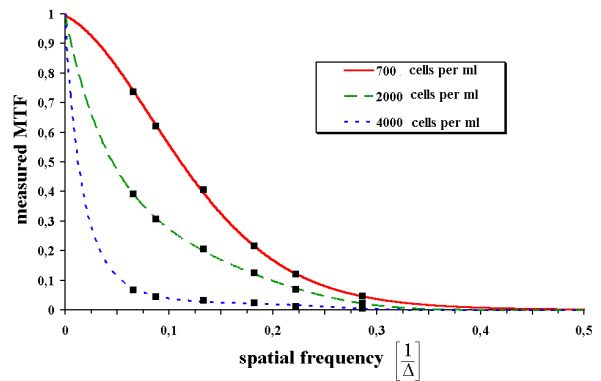


Fig. 15: Measured MTF with the alga *Scenedesmus acutus*

Fig. 15 shows the result of MTF measurements obtained with the alga *Scenedesmus acutus* at three concentrations. The mean diameter of these algae is $10 \mu\text{m}$. The spatial frequencies are given in units of $1/\Delta$, where Δ is the distance between two neighbouring pixels in the image. According to the Nyquist theorem the maximal detectable frequency is then 0.5Δ . The red curve, obtained with the lowest algae concentration, shows only a weak reduction of the amplitude of spatial frequencies, whereas the blue curve measured with the highest algae concentration yields the strongest reduction. Measured data are fitted with an exponential regression. The corresponding PSF, Fig. 16, is found by Fourier transformation.

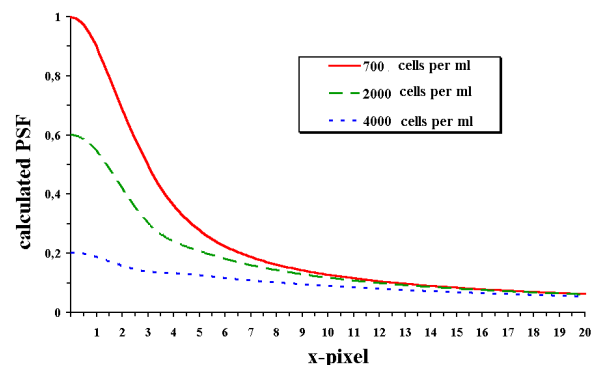


Fig. 16: Calculated PSF with the alga *Scenedesmus acutus*

Attenuation spectra of the water were measured to compare this parameter with the half-width of the PSF.

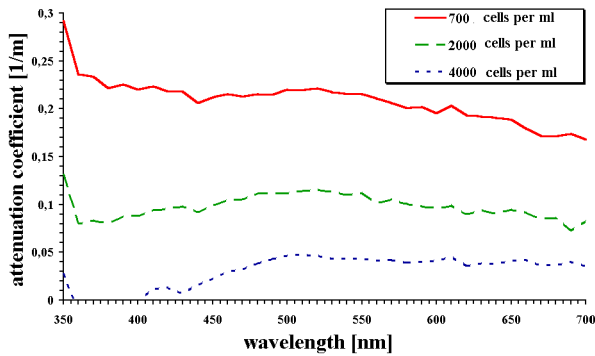


Fig. 17: Attenuation spectra of water samples with the alga *Scenedesmus acutus*

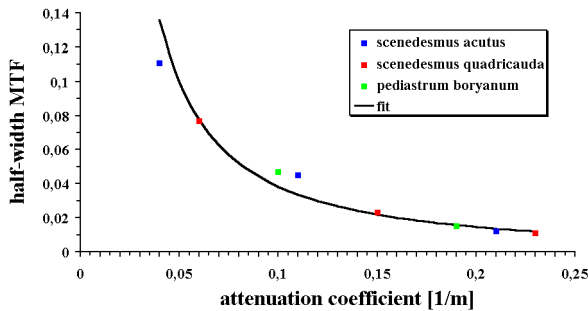


Fig. 18: Half-width of the MTF versus the attenuation coefficient at 532 nm wavelength.

5.3 Reconstruction of an underwater image

Fig. 19 shows the image of a test pattern recorded with the experimental setup described in section 5.1.

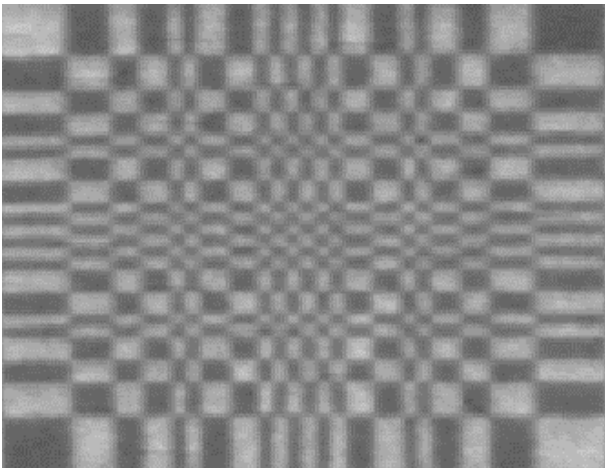


Fig. 19: Target at 10 m distance, gate-on time 5 ns

The image shown in Fig. 20 was restored with the Richardson-Lucy method and the D4 wavelet.

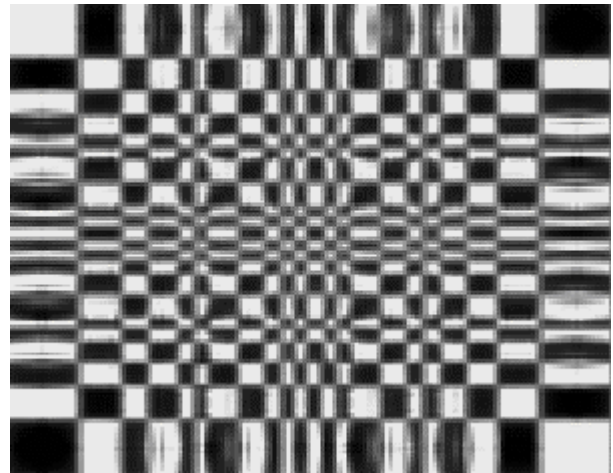


Figure 20: Result of the image restoration.

6. CONCLUSION

It has been shown that a restoration of a blurred underwater image using the PSF of the water column is possible. For an application of this technique the *in situ* determination of the PSF is required. Future research should focus on techniques for a direct and simple measurement of the PSF in water, and on the development of new algorithms to derive the PSF from other optical water properties which can be measured *in situ* [Barth et al., 1997].

The on-going evolution of computers and the development of faster and more efficient algorithms for image reconstruction should lead to real time applications of these methods in future.

8. ACKNOWLEDGEMENTS

The authors gratefully acknowledge the financial support of this project by the DLR Project Executive Department Environmental Protection and Technologies, Bonn, on behalf of the Federal Ministry for Research and Technology (BMBF), Germany.

9. REFERENCES

- H. Barth, K. Grisard, K. Holsch, R. Reuter and U. Stute, „A polychromatic transmissometer for *in situ* measurements of suspended particles and gelbstoff in water“, *Appl. Opt.* 36, 7919-7928, 1997
- S. M. Christie and F. Kvasnik, "Contrast enhancement of underwater images with coherent optical image processors", *Appl. Opt.*, Vol. 35, No. 5, 817-825, (1996)
- G. D. Gilbert, "The effect of particle size on contrast improvement by polarization discrimination for underwater targets", *Appl. Opt.* 9, 421-428, (1970)
- H. Gordon, "Equivalence of the point and beam spread functions of scattering media: a formal demonstration", *Appl. Opt.* 33, 1120 -1122, (1994)
- J. Jaffe, "The domains of underwater visibility", *Ocean Optics VIII, SPIE Vol. 637*, 287-293, (1986)

- L. E. Mertens, F. S. Replogle, "Use of the point spread function for analysis of imaging systems in water", *J. Opt. Soc. Am.*, Vol. 67, No.8, 1105-1117, (1977)
- W. H. Richardson, "Baysian-based iterative method of image restoration", *J. Opt. Soc. Am.*, 1972
- D. N. Sitter, J. S. Goddard and R. K. Ferrel, "Method for the measurement of the modulation transfer function for sampled imaging systems from bar-target patterns", *Applied Optics*, Vol. 34, No. 4, 746-751 (1995)
- J. L. Starck, F. Murtagh, "Image restoration with noise suppression using the wavelet transform", *Astronomy and Astrophysics*, 1994
- S. Svensson, J. Lexander, and B. Ericson, "Observation and inspection in Swedish waters", *Underwater Imaging, SPIE* Vol. 980, 75-81 (1988)
- Z. Ting-lu, L. Hai, "De-blurring the underwater image using the method of Monte Carlo", *Ocean Optics XII, Proc. SPIE* 2258, (1994)
- K. Voss, B. J. Frew "Aspects of the point spread function in coastal water", *Ocean Optics XIII, Proc. SPIE* 2963, 566-569 (1997)
- W. H. Wells, "Loss of resolution in water as a result of multiple small-angle scattering ", *J. Opt. Soc. Am.* 59, 686-691 (1969)